Ultrafast Flow Chemistry for the Acid-Catalyzed Conversion of Fructose

Pierre Desir[a,b], Basudeb Saha[b], and Dionisios G. Vlachos[a,b,*]

[a]*Department of Chemical and Biomolecular Engineering, University of Delaware, 150 Academy Street, Newark, Delaware 19716, United States*

[b]*Catalysis Center for Energy Innovation, 221 Academy Street, Newark, Delaware 19716, United States*

[*]Corresponding author

Email address: vlachos@udel.edu (D.G. Vlachos)

Abstract

Biomass conversion to chemicals and fuels has been epitomized by batch processing and long reaction times that limit the economic viability of future biorefineries and prevent modular manufacturing near the source-production site that is necessary due to the biomass' large water content. We introduce a continuous flow microreactor to enable process intensification and thousand-fold device miniaturization for remote chemical processing. We demonstrate the approach in the HCl-catalyzed fructose dehydration in water. We characterize and quantify the mixing using laser induced fluorescence (LIF) of fluorescent dyes and particle image velocimetry (PIV) of fluorescent microspheres. The estimated mixing times ranged from 0.03 to 4.8 s for residence times from 1 to 120 s, respectively. Moreover, a curved channel geometry induces secondary (Dean) vortices that produce a three-fold increase in mixing by diffusion through advection along the cross-sectional direction of the channel, creating dissipative chaotic mixing under laminar flow. We then obtain for the first time isothermal kinetics of fructose dehydration at short contact times and high temperatures and compare to a previous published, hybrid *ab initio* and data-driven kinetic model. Rigorous model optimization is carried out and an optimal HMF yield of 54% is attained in a single aqueous phase. High temperatures and low pH improve the reactor throughput by increasing the HMF space-time yield. We demonstrate the highest ever productivity (HMF yield per unit time). Importantly, this can be achieved at ~100% fructose conversion, eliminating the need for recycling to improve economics. Furthermore, optimization of the reactor dimensions and the specific energy dissipation rate result in ~60% pressure-drop related energy savings. We describe a methodology to scale-up microreactors to millimeter size and increase productivity 16-fold under optimal conditions. Energy efficiency and cost analysis for HMF production from corn stover of a typical corn farm indicate an optimal strategy for numbering-up millimeter size reactors and importantly, they underscore the potential feasibility of producing bioproducts in a distributed manner.

Keywords: Biomass, HMF, microreactor, continuous process, process intensification, chaotic mixing, reactor design, optimization

Broader context

Utilization of renewable carbon sources, especially non-food biomass (waste wood, energy crops and agricultural residues) is critical to ensure future energy security and mitigate the climate change. Current biomass processing technologies in batch systems involving multiple steps (for most bioproducts), poor heat and mass transport, complex and expensive separation steps, and high CapEx pose a major bottleneck toward economic production of biochemicals and biofuels. Transportation costs of high volume biomass to the processing sites make the economics worse. Distributed, modular manufacturing of bioproducts in the vicinity of biomass supply chain, using compact and portable devices with short reaction times, and better energy-efficiency and productivity can enable cost-competitive production of bioproducts compared to conventional chemicals and fuels. We demonstrate for the first time that sugar dehydration can be processed isothermally in a microreactor of diameter 500 μm at ultrashort contact time and with 2 – 3 orders of magnitude greater heat and mass transfer rates than the batch systems, achieving the highest ever productivity of HMF reported to-date. Further, our quantitative conversation of sugar can eliminate the need for its downstream separation and recycling, thus improving the process economics. The process concept and the methodology for characterization and quantification of mixing introduced herein will have a significant impact on cost-competitive production of various bioproducts to render biorefineries viable.

Introduction

The continuous depletion of natural oil resources and sustainability concerns associated with the current industrial processes for fuel and petrochemicals production necessitate alternative, greener routes for energy production and chemical manufacturing. During the past decade, efforts have been devoted to using ligno-cellulosic biomass (wood chips, corn stover, switchgrass, etc.) as a renewable source of energy and chemicals. The C5 and C6 sugars obtained from biomass hydrolysis often undergo Brønsted acid catalyzed dehydration to produce platform chemicals. One such platform is the 5-hydroxymethyl furfural (HMF), usually obtained from the dehydration of C6 sugars, such as glucose and fructose. HMF can be converted to 2,5-dimethyl furan (DMF), a potential fuel additive, through hydrodeoxygenation over various carbon-supported metals (Pd[1-3], Pt[1], Ru[1-4], Rh[1], Cu[2, 3]), metal oxides[5], and Pt-Co nanoparticles[6]. Furthermore, HMF and its furanic derivatives can be used for the production of para-xylene over H-Y[7-13], Na-Y[7, 12], H-ZSM-5[13], H-BEA[9, 10, 14] and other beta zeolites substituted with metals such Zr, Sn, Ti[15, 16], Al, Ga, Fe or non-metals like B[17] and P[18]. Other HMF-derived products include dienes[19], detergents[20], 2,5-furandicarboxylic acid (FDCA), an alternative to polyethylene terephthalate (PET)[4, 21-23], and lubricants[24]. This diversification to fuels and chemicals is expected to significantly increase economic viability of biorefineries. An essential step in this sequence of reactions is the acid-catalyzed dehydration of fructose to HMF. Fructose dehydration has been extensively studied using various heterogeneous catalysts, H-BEA[25, 26], Sn-BEA[27-29], TiO_2[30-32], ZrO_2[31-33], Amberlyst-15[34-37], etc. or more commonly, inorganic Brønsted acids, such as HCl, H_2SO_4, and H_3PO_4. In parallel with the main reaction, side-products form from the acid rehydration and polymerization of HMF (levulinic acid (LA) and formic acid (FA) and humins, respectively)[29, 38-41]. Thus, the yield and selectivity to HMF in water is usually low.

Biomass processing is typically demonstrated in batch systems with reaction times often spanning several hours. The high volume of biomass requires continuous processing for economic viability. Furthermore, the large water content requires processing within a radius of 50 or so miles from the source[42-45]. This local-to-the source processing, known also as chemical plant on wheels, requires compact, portable devices and ultrashort processing times. Ultrashort processing times in turn require high temperatures that make batch systems unsuitable due to slow heat transfer. As a result, this operating regime of high temperatures/ultrashort processing time is unattainable in typical batch systems. In order to overcome the limitations of batch systems, continuous flow microreactors can be employed for process intensification. Microstructured reactors usually consist of channels of a characteristic diameter <1 mm. Due to their small diameter, these systems possess high surface-to-volume ratios, and 2 – 3 orders of magnitude greater heat and mass transfer rates than batch reactors. In turn, this allows us to operate at high temperatures and very short residence times. Thereon, tight operating windows can be achieved with precise control of process conditions and low or no transport limitations[46, 47]. Importantly, microreactors often lead to higher yields and selectivities than large batch systems at shorter residence times because of the fast diffusive mixing[48]. Yet, the application of microreactors to biomass processing has been scarce. For example, in the past 5 years, out of 566 papers published, 560 used batch reactors and only 6 employed microreactors for HMF synthesis from fructose (Figure S1, ESI). Comparison of our technology to relevant flow microsystems is given below.

A few reports have exploited microreactors for the single-phase dehydration of fructose to HMF. Aida and coworkers studied fructose dehydration in subcritical water with no added catalyst at temperatures 350 to 400 °C[49]. Under the intrinsic acidic conditions of water, fructose dehydration led to ~7% HMF yield due to degradation and condensation reactions at residence times less than 1 s. Tuercke *et al.*[46] optimized the HMF yield with respect to reaction temperature at a fixed residence time of 1 min and obtained up to 53% HMF yield with improved selectivity compared to batch reactors. They attributed the enhanced selectivity to a steep heating profile and improved mass transfer and mixing characteristics resulting from passive mixers embedded along the microchannel. Yet, no systematic characterization of the heat and mass transfer was conducted. Hansen *et al.* obtained up to 53% HMF yield at 95% fructose conversion using HCl as the catalyst at 200 °C and a reaction time of 1 min[50] using microwave heating. To our knowledge, reaction times of seconds or shorter have not been reported in continuous systems for biomass processing using conventional heating.

The aim of this paper is to introduce continuous flow chemistry for lignocellulosic biomass processing at residence times of seconds or lower. This in turn can enable modular chemical manufacturing. We demonstrate our approach for the aqueous-phase dehydration of fructose to HMF using HCl as the catalyst. We use fructose as a demonstration case since short time scales are not suitable for fermentation and in general low temperature biological processes applied to the production of bioethanol, and fructose dehydration is one of the most well-established chemistries that can be benchmarked against conventional production systems. Herein, we characterize the temperature uniformity and mixing to ensure adequate heat and mass transfer necessary to obtain intrinsic kinetics. We then conduct a kinetic study of the fructose dehydration and compare it to a hybrid first-principles/data-driven kinetic model. We also determine the

optimal operation conditions and microchannel size that maximize the HMF yield and reduce energy dissipation. In addition, we develop a methodology to assess the scalability of the microreactor along with an analysis of the overall energy efficiency and relative cost for HMF production under optimal reaction conditions.

Materials and Methods

Materials

Two Waters 515 High Pressure Liquid Chromatography (HPLC) pumps (Waters Alliance) or two syringe pumps (Harvard Apparatus PHD2000) were used to pump the liquid feeds. Perfluoroalkoxy alkane (PFA) tubing (Idex Health) with ID = 500 μm and OD = 1600 μm was used for the microreactor. Fluid connections were made using 1/16" polyether ether ketone (PEEK) unions (Valco Instruments), 1/8" to 1/16" PEEK reducing unions (Valco Instruments), and a 1/16" PEEK tee (Valco Instruments). A 1/16" PEEK cross (Valco Instruments) was also used as a micromixer in the microreactor setup. K-type thermocouples (OD = 0.02") (Omega Engineering) were used to measure the fluid temperature along the reactor. Teflon tape (Fisher Scientific) was used to coat the thermocouple probes and prevent corrosion by the acid solution. A 2 μm pore inline filter (Idex Health) was also used to filter out the solid particles formed in the microchannel. A back-pressure regulator (Idex Health) was used to maintain the reacting mixture liquid at high temperatures. Sodium fluorescein 99% (Sigma Aldrich), 2 μm green fluorescent poly lactic-co-glycolytic acid (PLGA) (Sigma Aldrich) microspheres, and deionized water (Milli-Q) were used for flow visualization and mixing characterization. D-fructose 99% (Sigma Aldrich), FA 88% (Fisher Scientific), LA 98% (Sigma Aldrich), HMF 98% (Sigma Aldrich), HCl 37% (Fisher Scientific), KCl 99% (Sigma Aldrich), and deionized water (Milli-Q) were used to prepare solutions.

Analytical Methods

The mixing and hydrodynamics in the microreactor were evaluated using laser induced fluorescence (LIF) of sodium fluorescein dye with a high-speed confocal microscope (Highspeed LSM 5 Live Duo) mounted with an inverter and syringe pumps for the feeds, as shown in Scheme 1. The mixing was quantified by measuring the degree of segregation in the intensity profile during the dilution of a 250 μM sodium fluorescein dye with deionized water by image processing in ImageJ. Furthermore, flow and mixing patterns were determined by particle image velocimetry (PIV) using a solution of PLGA microspheres (1×10^9 spheres/mL) by image processing in MatLab, using PIVLab[51].

Reaction kinetics were measured by identifying and quantifying the reactants and products using HPLC (Water Alliance Instruments). Fructose, FA, LA, and HMF were detected by a Biorad HPX 87H column heated to 50 °C and 0.005 M sulfuric acid flowing at 0.5 mL/min as the mobile phase. Fructose, FA, LA, and HMF eluted at 12.4, 17.2, 19.8, and 38.5 minutes, respectively. Additional small peaks indicated negligible amounts of other condensation and degradation reaction products, which were not quantified.

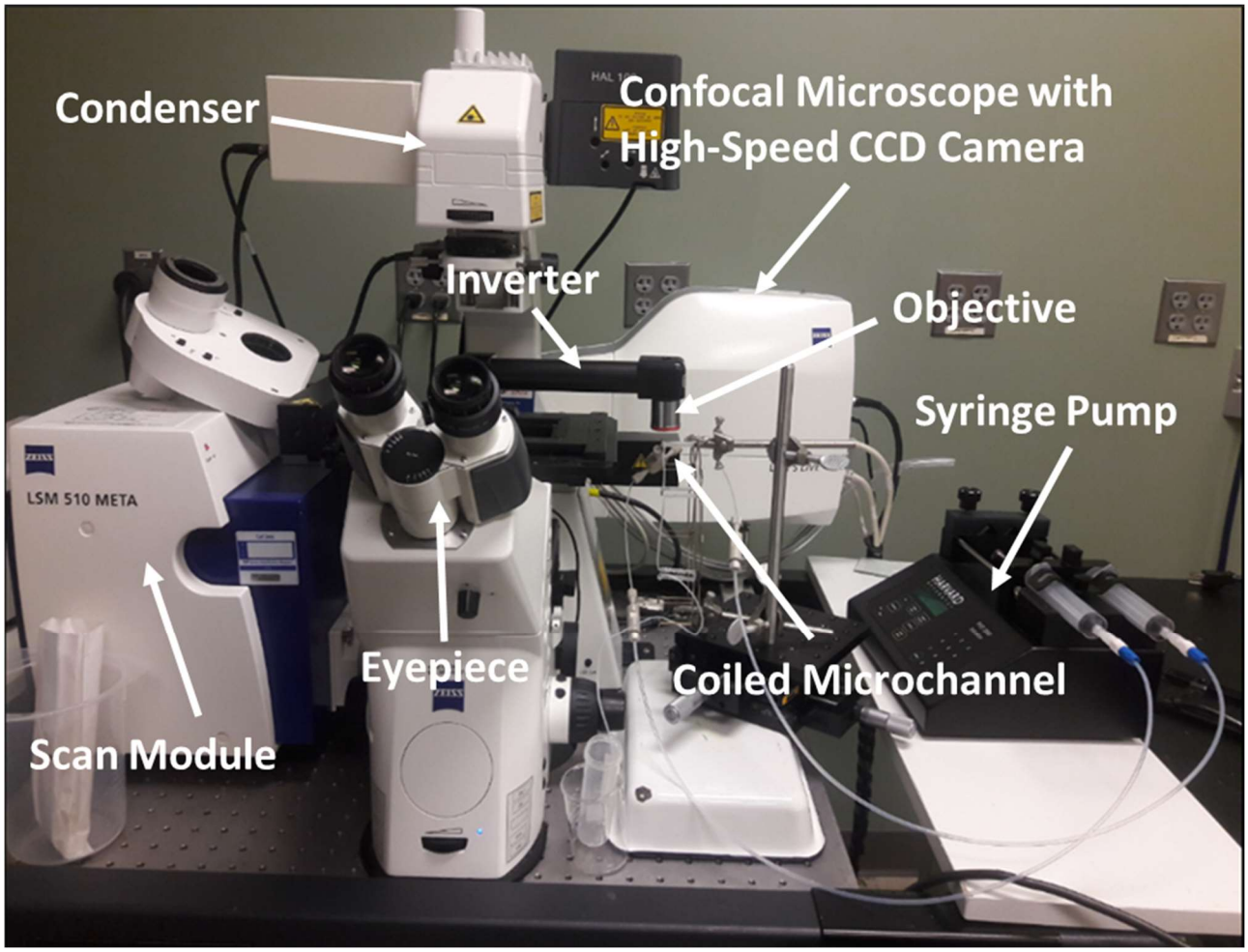

Scheme 1: Overview of the setup of the high-speed confocal microscope with an inverter placed on top of the microchannel connected to the syringe pumps.

Computational Methods

The kinetic model of HCl-catalyzed fructose dehydration developed by Swift *et al.*[40] was used. The model is based on the reaction network shown in Scheme 2 and considers fructose dehydration to HMF (R_1), fructose degradation to humins (R_2), HMF rehydration to LA and FA (R_3), HMF degradation to humins (R_4), and fructose degradation to FA and humins (R_5).

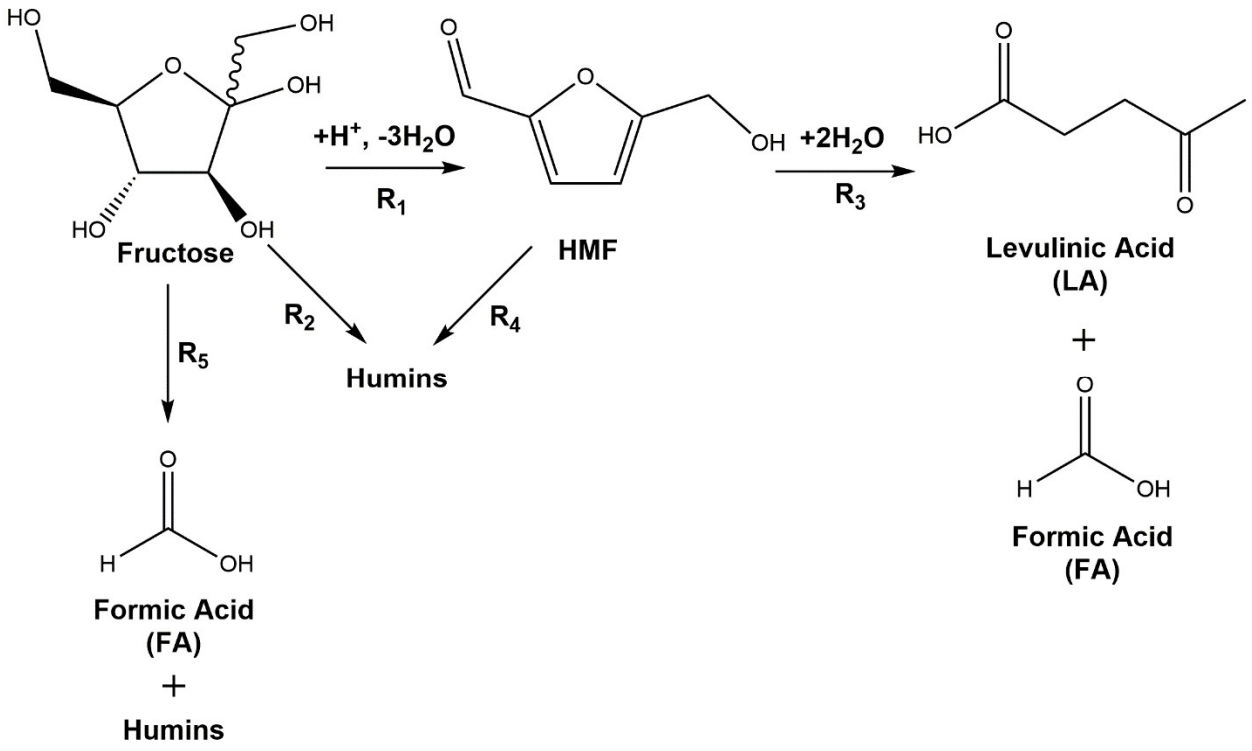

Scheme 2: Reaction network for HCl-catalyzed fructose dehydration to HMF developed by Swift *et al.*[40].

The dehydration reaction network was studied with Quantum Mechanics/Molecular Mechanics (QM/MM) [52], and free energies were estimated for the microkinetic model[53]. Results were compared to batch experimental data at low temperatures and long reaction times. In the work of Swift *et al.*[40], the kinetic parameters of the degradation steps were determined from data in a batch reactor at temperatures ranging from 74 to 150 °C. A PFR model was used to approximate the microreactor. The model equations and reaction rates are given by:

$$\frac{dC_i}{d\tau} = \sum_{j=1}^{4} \alpha_{ij} R_j \tag{1}$$

$$R_1 = k_1 \varphi_f C_{Fru} \left(\frac{K_{DH} C_{H^+}}{C_{H_2O}} \right) \tag{2}$$

$$R_2 = k_2 C_{Fru} C_{H^+} \tag{3}$$

$$R_3 = k_3 C_{HMF} C_{H^+} \tag{4}$$

$$R_4 = k_4 C_{HMF} C_{H^+} \tag{5}$$

$$R_5 = k_5 C_{Fru} C_{H^+} \tag{6}$$

Here, C_i is the concentration of component i, R_j is the reaction rate of reaction j, α_{ij} is the stochiometric coefficient of component i in reaction j, τ is the residence time, $k_1 - k_5$ are the respective reaction rate constants, K_{DH} is the dehydration equilibrium constant and φ_f is the equilibrium fraction of fructose in the furanose form (fructose tautomer). The values for the kinetic parameters can be found in the work of Swift *et al.*[40]

Microsystem Setup

Scheme 3 shows a schematic and a picture of the continuous flow microreactor setup. Two HPLC pumps separately pump a 2.6 wt% aqueous fructose solution and a HCl/KCl buffer solution (pH varying from 0.7 to 1.6) as catalyst at a total flow rate (Q_{total}) ranging from 0.1 to 10.4 mL/min. The catalyst feed is preheated to the reaction temperature (170 – 200 °C) inside a gas chromatography (GC) oven. The fructose feed flows at room temperature and is then mixed with the hot acid feed at the entry port of the GC oven. The mixing of the solutions occurs via a PEEK cross serving as a T-shaped micromixer. After mixing, the reacting solution flows through a 1 m coiled PFA capillary microchannel with circular cross-section (ID = 500 μm) where the reaction occurs. A coiled channel geometry with a coil diameter of 1 mm was chosen to induce continuous passive mixing throughout the reactor operating in laminar flow. Two K-type thermocouples (T_{inlet} and T_{outlet}) coated with Teflon were inserted at the inlet and outlet of the microchannel, respectively, to measure the fluid temperature within ± 0.1 °C. Experiments were initially conducted to evaluate the temperature uniformity under the shortest reaction time and highest reaction temperature considered in the kinetic study (Figure S2 and Figure S3, ESI). A volumetric flow rate ratio between the HCl and the fructose feed solutions (HCl/fructose (v/v)) of 25 assured fast heating of the fructose stream by mixing it at the reactor inlet with the HCl stream preheated to the reaction temperature. Mass and energy balances can be used to design the system so that the mixing length for temperature equilibration is short (Scheme S1, Scheme S2, Table S1, Table S2, and Figure S4, ESI). This volumetric flow rate ratio between the two streams is kept fixed to minimize the effect of temperature gradients on kinetics. The change in density with temperature is relatively small and thus, herein we do not distinguish contact time from residence time. A back-pressure regulator is placed further downstream to pressurize the reacting mixture up to 17 bar. The reactor operating pressure is considerably lower than the maximum pressure rating (138 bar) of the microchannel wall material. Thus, reaction temperatures greater than 200 °C can possibly be achieved while maintaining a liquid-phase reaction. After reaction, the products leaving the microchannel are quenched into an ice bath and are filtered through an inline filter before being collected for further analysis.

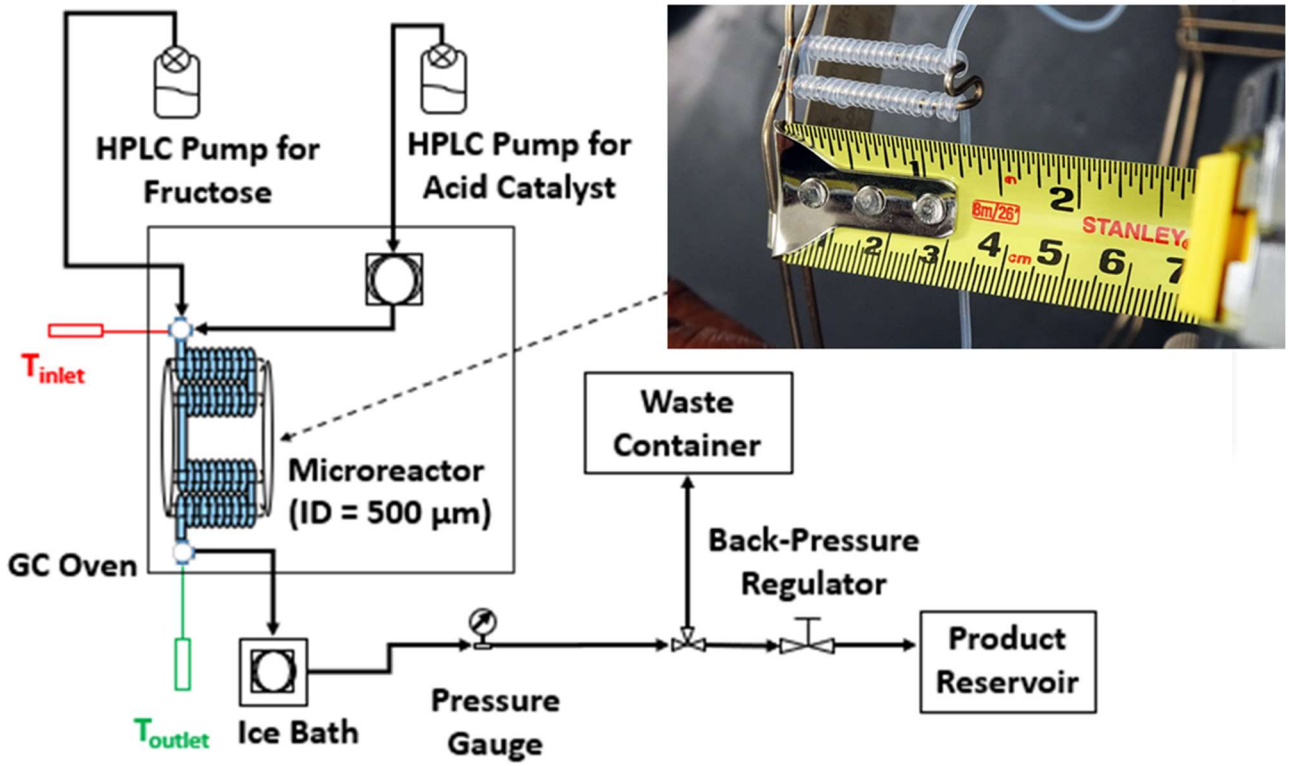

Scheme 3: Schematic overview of the microreactor setup.

Results and Discussion

Mixing Characteristics of Coiled Microchannel

The degree of mixing[54, 55] was quantified by calculating the percent of mixing of a concentrated sodium fluorescein (Fl) feed with a deionized water feed. The mixing percent is then determined by measuring the degree of segregation in the intensity profile of a sodium fluorescein dye solution diluted with deionized (water/Fl (v/v) = 25) water at various cross-sections and flow rates along the microchannel (Figure S5, Figure S6, and Figure S7, ESI). In order to describe the effects of curvature on mixing, we calculate the Dean (De) number, defined in terms of the Reynolds number (Re) for a given flow rate:

$$Re = \frac{\rho U d_H}{\mu} \tag{7}$$

$$De = Re\sqrt{\frac{d_H}{2R}} \tag{8}$$

where ρ is the density of the fluid, U is the linear speed of the fluid, μ is the viscosity of the fluid, d_H is the hydraulic diameter of the channel, and R is the radius of curvature of the channel.

The fluid is subject to centrifugal acceleration towards the outer radial direction due to the curvature, leading to transverse velocity components and the formation of secondary vortices known also as Dean vortices[56, 57] whose intensity is described by the Dean number. As they grow in intensity, the vortices generate chaotic (enhanced) mixing under laminar flow by stretching and folding of the fluid streamlines. Figure 1a shows the mixing percent as a function of De and flow rate, at different distances along the coiled microchannel. At a given distance, a minimum in mixing occurs at De = 13 with increasing De or flow rate. For a fixed De, mixing increases with increasing distance along the microchannel and complete mixing is achieved at all flow rates 6 cm downstream of the inlet. De = 13 underscores the onset of Dean flow where counter-current secondary vortices are induced by centrifugal forces. For De < 13, the axial convective time decreases relatively to the characteristic diffusive time with increasing De or Re number, reducing the extent of mixing (diffusion-limited mixing)[58]. For De > 13, secondary vortices form that exponentially increase the interfacial area for mixing with increasing Re or De, enhancing mixing (advection-limited mixing regime)[58]. By comparing the mixing in the coiled microchannel to that of a straight one under similar flow conditions, up to three-fold enhanced mixing occurs due to the Dean vortices (Figure S8, ESI).

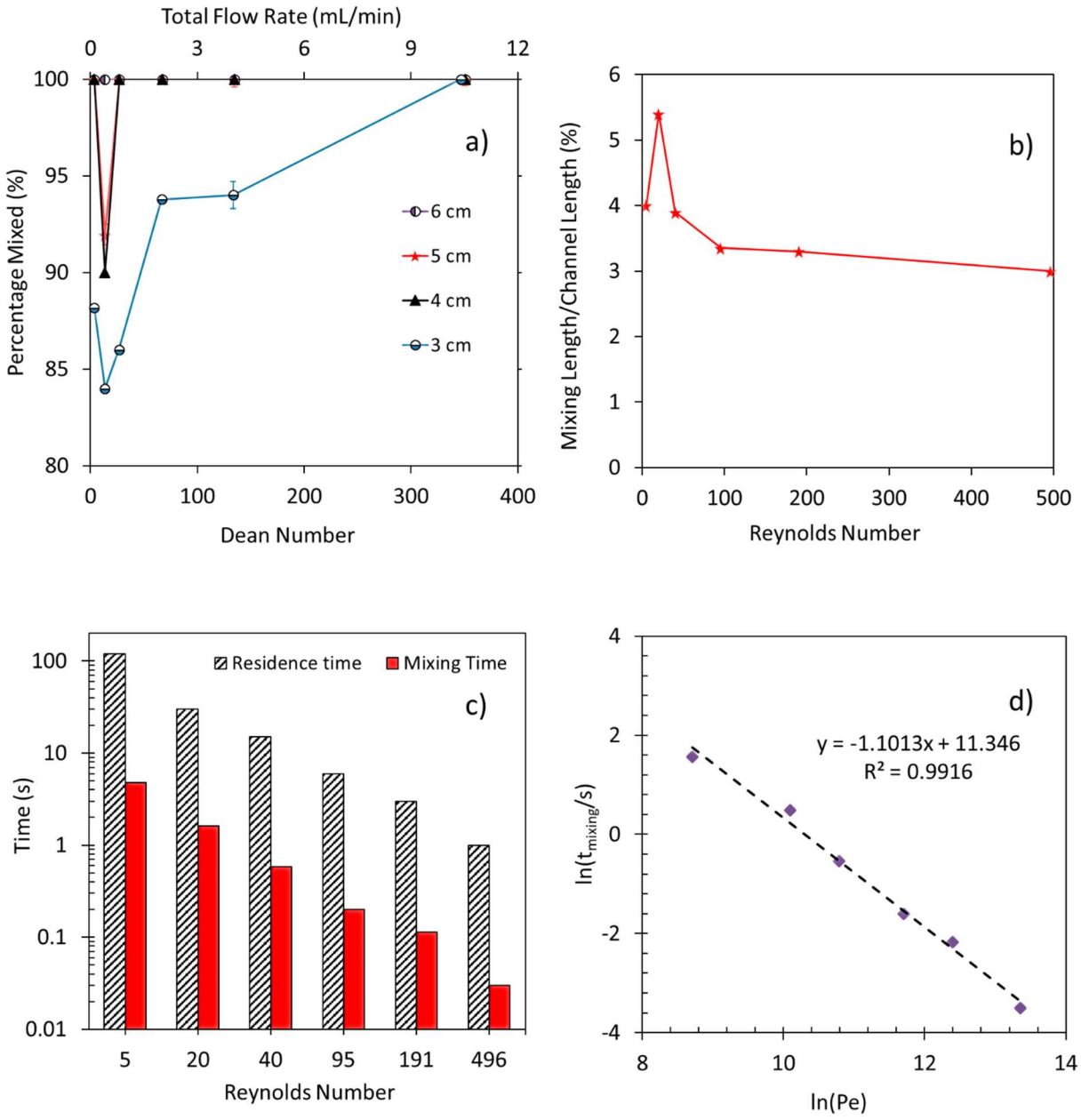

Figure 1: Mixing characteristics of the microreactor: mixing percent (a) as a function of the Dean number; normalized mixing length (b) and residence and mixing times (c) vs. Reynolds number; mixing time (d) vs. Péclet number. Conditions: water/Fl (v/v) = 25, microreactor length = 1 m.

The mixing length was determined by graphically obtaining the distance at which the mixing percent reaches ~100%. Figure 1b plots the normalized mixing length as a function of *Re* number. As the *Re* number increases, the mixing length initially increases up to 5.5% of the actual

microchannel length, and then decreases down to 3% at higher Re values. The maximum observed in the mixing length occurs at the same Re or De where the transition from a diffusion-limited to the advection-limited regime takes place. Figure 1c demonstrates the fast mixing characteristics of the microreactor with mixing times ranging from 0.03 to 4.8 s at respective residence times from 1 to 120 s. Several literature reports have shown that the mixing time is a function of the Péclet (Pe) number in the chaotic mixing regime[59-62]:

$$Pe = \frac{U d_H}{D_{diff}} \tag{9}$$

Herein, D_{diff} is the diffusivity of the solute used during the mixing studies. In the fully chaotic flow regime, $t_{mixing} \propto \ln(Pe)$, whereas in the partially chaotic regime, $t_{mixing} \propto Pe^{\alpha}$. The coefficient α is related to the mean value of the finite time Lyapunov exponent, which describes the degree of chaotic mixing and the type of chaotic flow[63]. Figure 1d correlates the mixing time vs. the Péclet number. The correlation implies that the microreactor operates under partially chaotic mixing. The value of α of -1.013 indicates a chaotic dissipative flow where the fluid elements flow in an orbital motion attracted to a fixed point[64, 65]. This behavior is a direct consequence of the coiling of the microchannel exhibiting attractive centripetal forces towards the center of each coil.

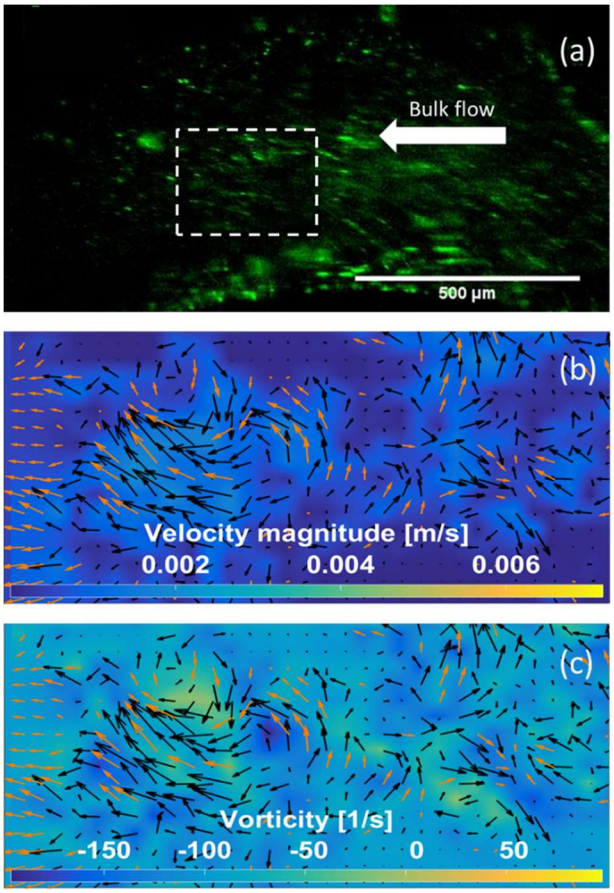

Figure 2: Imaging of the flow of PLGA microspheres in the coiled microchannel (a) and PIV results of the velocity vector field (b) and the vorticity (c). The dashed squared lines in (a) delineate the small test section of the microchannel curvature for which the velocity vector field in (b) and the vorticity field in (c) are generated. The bulk flow is from right to left. Conditions: Q_{total} = 2 mL/min, De = 95, distance = 35 cm (32nd coil).

Figure 2a shows PIV results for the flow of PLGA microspheres in the coiled microchannel, with the bulk flow moving from left to right. The velocity vector field (Figure 2b) clearly shows that the particles move in circulating patterns along the cross-section. Figure 2c shows the vortices around the curvature of the channel. The vorticity takes positive and negative values, characteristic of counter-current secondary vortices (clockwise and counter-clockwise rotation). Vortex formation induces stretching and folding of fluid filaments along the cross-section, which creates chaotic, enhanced mixing in laminar flow. Our PIV measurements directly and visually support the presence of Dean vortices.

Kinetics of Fructose Dehydration

Given the temperature uniformity and fast mixing, the coiled microchannel is ideal for extracting kinetics at short residence times. To our knowledge high temperatures while ensuring that the reactor is practically isothermal have not been achieved in prior biomass processing. Figure 3 compares the experimentally measured and model predicted performance of the microchannel. Overall, good agreement is found without adjustments in model parameters despite the significant extrapolation of the model (Figure S9, ESI). At a given temperature, the fructose conversion increases with increasing residence time and the HMF yield reaches a maximum, consistent with HMF undergoing side-reactions to LA, FA, and humins. Furthermore, the HMF selectivity decreases slightly at first with increasing fructose conversion and sharply at high conversions, as fructose degradation to FA and humins also occurs at higher conversions. The nearly constant HMF selectivity is due to the activation energy for the fructose degradation to humins (135 kJ/mol[40]) and to FA and humins (130 kJ/mol[40]) being comparable to that of the fructose dehydration to HMF. Moreover, as the fructose conversion increases with temperature, the maximum HMF yield also increases, due to the activation energies for the HMF degradation reactions (97 kJ/mol[40] for the formation of LA and FA and 62 kJ/mol[40] for the formation of humins) being smaller compared to that for fructose dehydration to HMF (126 kJ/mol[40]), consistent with previous studies[66, 67]. These results prove that operation at high temperatures improves HMF production giving an optimal HMF yield of 54% at nearly complete fructose conversion (magenta line and data in Figure 3). Complete substrate conversion while achieving maximum HMF yield eliminates separation of fructose from the product stream and the need to recycle the sugar and can significantly improve process economics. To our knowledge, this is the first time that high HMF yield is reported at 100% fructose conversion. This is achieved at a residence time of a few seconds. Operation at higher temperatures are expected to further decrease the residence time to ultrashort (<1 second) values (see below).

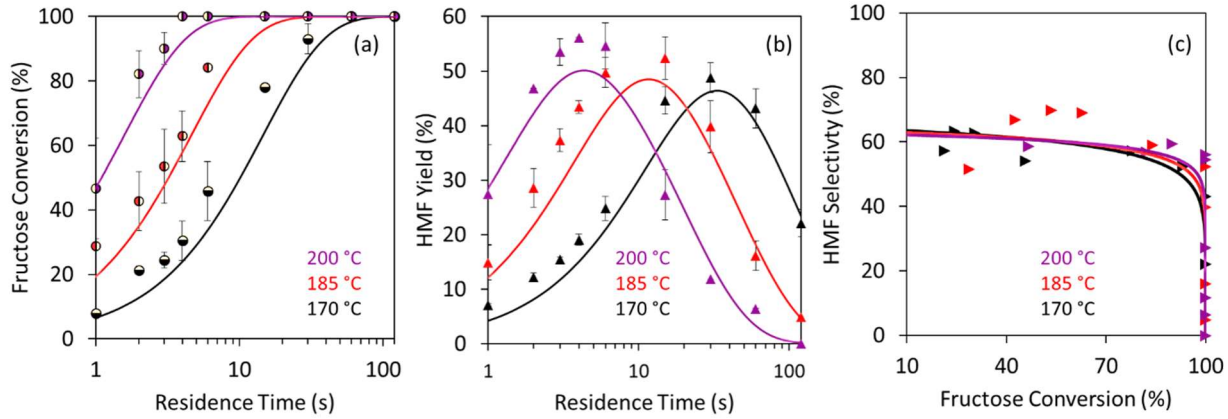

Figure 3: Temperature effect on the time-profiles of fructose conversion (a) and HMF yield (b). HMF selectivity relative to fructose conversion (c). HCl/KCl buffer solution as the catalyst with pH = 0.7 and 0.1 wt% fructose inlet concentration in a single (aqueous) phase. Points are experimental measurements and lines are (unadjusted) model predictions. High conversion can lead to low or high selectivity and yield, depending on operating conditions (data along the right, vertical axis of panel c).

The effects of fructose loading on the optimal HMF yield were also studied and the results show that the fructose conversion and the HMF yield and selectivity remain unchanged with fructose inlet concentrations from 0.1 to 5 wt% (Figure S10, Figure S11, ESI). Experimental and computational data on the effect of catalyst concentration (variable pH) on the dehydration kinetics at 200 °C are shown in Figure 4. The agreement is again very good. For a given pH, the fructose conversion increases with increasing residence time. A maximum in the HMF yield is still observed while the HMF selectivity decreases slightly at first and then sharply with increasing fructose conversion. Lower pH values enhance the conversion while maintaining the maximum obtainable HMF yield because they accelerate the degradation reactions equally, as reported elsewhere[41, 68]. Importantly, low pH values lead to very high conversions at very ultrashort residence times, leading to significant process intensification.

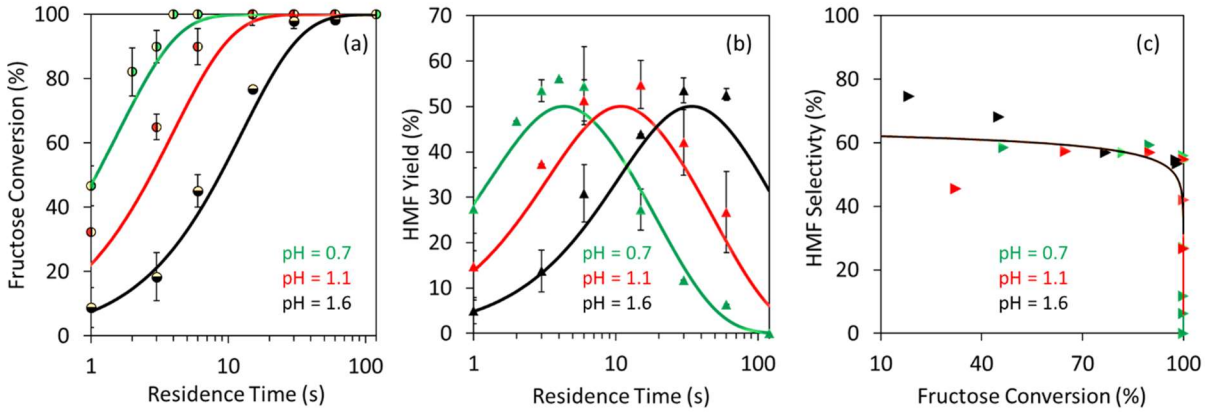

Figure 4: pH effect on the time-profiles of fructose conversion (a) and HMF yield (b) and HMF selectivity relative to fructose conversion (c) using an HCl/KCl buffer solution as the catalyst and 0.1 wt% fructose inlet concentration at 200 °C. Points are experimental measurements and lines are (unadjusted) model predictions. High conversion can lead to low or high selectivity and yield, depending on operating conditions (data along the right, vertical axis of panel c).

Two recently published papers employed biphasic microreactors using reactive extraction with methyl isobutyl ketone (MIBK) as the organic/extracting phase. Specifically, Zhou and coworkers[69] studied a dripping flow microreactor that used a microporous membrane to generate dispersed MIBK droplets in water. A yield of 93% HMF was obtained at 180 °C and a residence time of 4 min. Although the authors characterized the flow patterns in the microreactor, mass transfer between the two phases, which is key in designing biphasic microreactors, was only described by evaluating the extraction efficiency during dehydration. Lueckgen *et al.*[70] conducted reactive extraction of HMF from fructose in a water/MIBK slug flow microreactor. The optimum HMF yield was 91% at 150 °C and a residence of 40 s. The fluid dynamics of the slug flow and the mass transfer between phases were not characterized. Although direct comparison cannot be made between our work in the monophasic microreactor and these biphasic studies, our approach in thoroughly designing the microreactor allows us to reduce the processing time by a factor of 10 – 60 when compared to these biphasic microreactors. Thereon, our work lays down the

foundational ground in developing design tools for fast biomass processing and can be leveraged in improving the reactive extraction in biphasic microreactors. As elaborated below, our approach enables design of optimal systems that can enable distributed manufacturing at reasonable cost.

Optimal Microchannel Performance

Since the model adequately describes the microreactor, we used the model predictions to optimize the HMF yield.

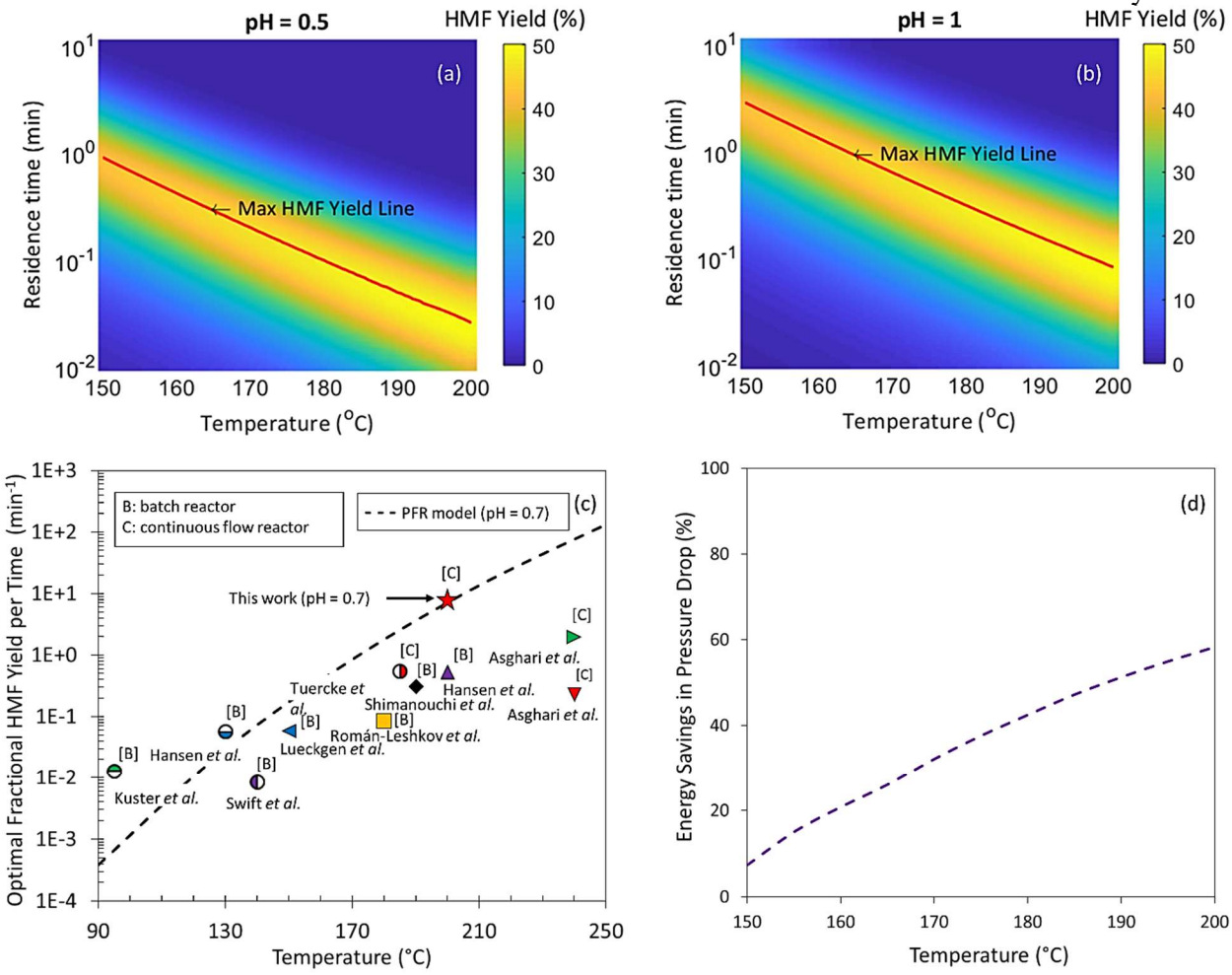

Figure 5a and b present the model predictions of HMF yield as heat maps of temperature and residence time. As the reaction temperature increases at fixed pH, the maximum HMF yield increases and the residence time decreases. At lower pH values, the maximum HMF yield is the same at a given temperature but the residence time decreases. Consequently, the model predicts that high temperatures and low pH values improve the HMF space-time yield in the reactor and thus the reactor throughput. Overall, the model predicts that the optimal HMF yield obtainable in a single aqueous phase is ~50%. This finding is in close agreement with the optimal experimental HMF yield of 54% observed in our microreactor and Hansen *et al.*'s findings (an HMF yield of

53% at 95% fructose conversion at 200 °C[50]). Further increase in temperature indicates relatively small increase in HMF yield (53% at 300 °C; new degradation side-reactions that are unaccounted for in the kinetic model may become relevant at these temperatures). Importantly, optimal attainable region (yellow regime around the red lines) is fairly broad indicating that small perturbations in flow rate or temperature control would not affect performance, i.e., the optimal operation is rather robust.

In order to evaluate the productivity of our microreactor, we evaluated the experimental HMF fractional yield per time defined as:

$$Fractional\ Yield\ per\ Time = \frac{HMF\ Concentration}{Fructose\ Initial\ Concentration \times Residence\ Time} \quad (10)$$

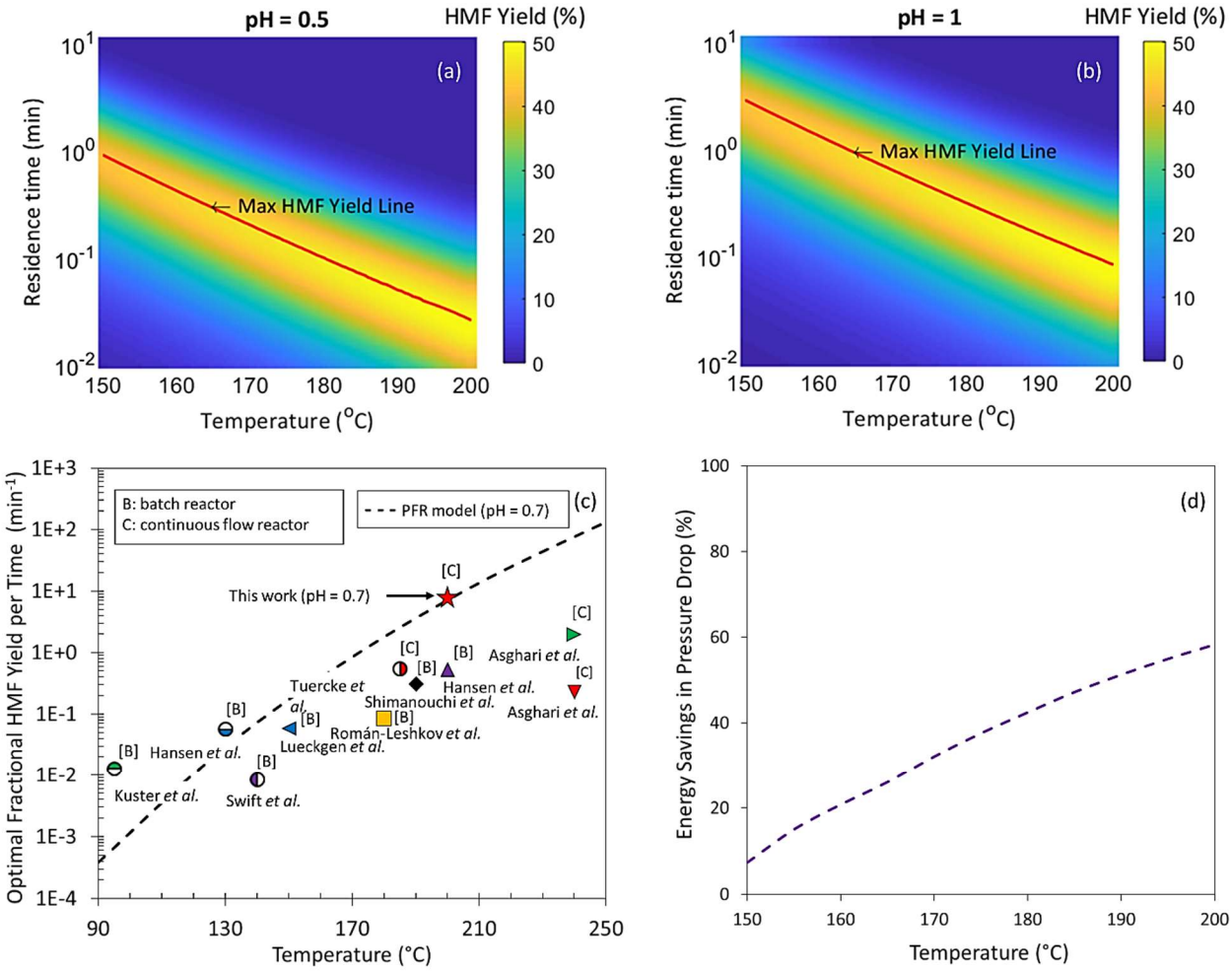

Figure 5c plots the optimal HMF fractional yield per time as a function of temperature, for our microreactor and various literature reports[40, 46, 50, 71-73]. Overall, the optimal fractional yield per time in our microreactor exceeds the values reported in other literature works by 10- to 1000-fold. Studies performed by Tuercke *et al.*[46] (54% HMF yield at 180 °C) and Hansen *et al*.[50] (53% HMF yield at 200 °C) show yields similar to our microreactor (54% HMF yield at 200 °C). Nonetheless, both of those works report optimal yield at a reaction time of 1 min as opposed to our microreactor that operates at 4 s. To our knowledge, the shortest reported reaction time of 10 s at 240 °C for a considerably lower HMF yield of 33% was reported by Asghari *et al*.[73]. It follows from the published studies that high HMF yields were obtained at the expense of longer reaction times, but such an approach hinders the overall productivity. Although the absolute optimal yield in the microreactor is comparable to the highest reported before, the improvement in productivity is a direct consequence of the ultrashort reaction times enabled by the fast mixing (mixing times that are merely 3 – 5.5% of the reaction times) and isothermal operation at elevated temperatures, conditions that are challenging to reach in conventional batch and continuous systems, e.g., it takes 20 min to 1.5 hr to heat up laboratory batch reactors of 50 mL to 1 L using external heating, making them poor for kinetics studies and short contact time production, as accomplished herein. Moreover, while lab-scale Parr reactors usually have fast internal mixing, industrial size batch reactors are more prone to dead zones and suffer from slower external heat transfer rates for liquid phase reactions, further hindering the productivity.

Next the microchannel dimensions and the pressure drop are evaluated. The latter is of particular interest as these capillary microchannels are often subject to high pressure-drop due to their small diameter. The aim is to determine the reactor length (constant diameter) and flow rate that minimize the pressure drop and maximize the energy savings to produce the maximum yield of HMF at a fixed temperature and pH. Firstly, using the kinetic model at the set temperature and pH, we determine the residence time required to achieve the maximum yield of HMF. Secondly, we set that the mixing time is <5% of the residence time. Thereon, we estimate mixing times in the range of flow rates considered in this study using the correlation obtained from Figure 1d. The optimal flow rate is then taken as the lowest flow rate for which the estimated mixing time satisfies the criterion for good mixing. Furthermore, the optimal reactor length is estimated such that the required residence time is met. Thirdly, considering the geometry of the microchannel formed by alternating segments of coiled and straight tubing, we evaluate the specific energy dissipation, ε, associated with the pressure drop:

$$\varepsilon = \frac{8 f L_R {Q_{total}}^2}{\pi^2 {d_i}^5 \tau} \tag{11}$$

where f is the Darcy friction factor, L_R is the microreactor length, and d_i is the internal diameter of the microreactor. Lastly, we calculate the energy savings from optimizing the reactor length and energy dissipation relatively to our nominal microreactor system with fixed channel length of 1 m, operating under the same conditions to produce the maximum HMF yield. The energy savings, E, are obtained from:

$$E = \left(1 - \frac{\varepsilon_{opt}}{\varepsilon_{nom}}\right) \times 100\% \qquad (12)$$

for which ε_{nom} is the specific energy dissipation due to pressure drop of the nominal microreactor under the conditions to achieve the maximum HMF yield and ε_{opt} is the energy dissipation with optimized dimensions.

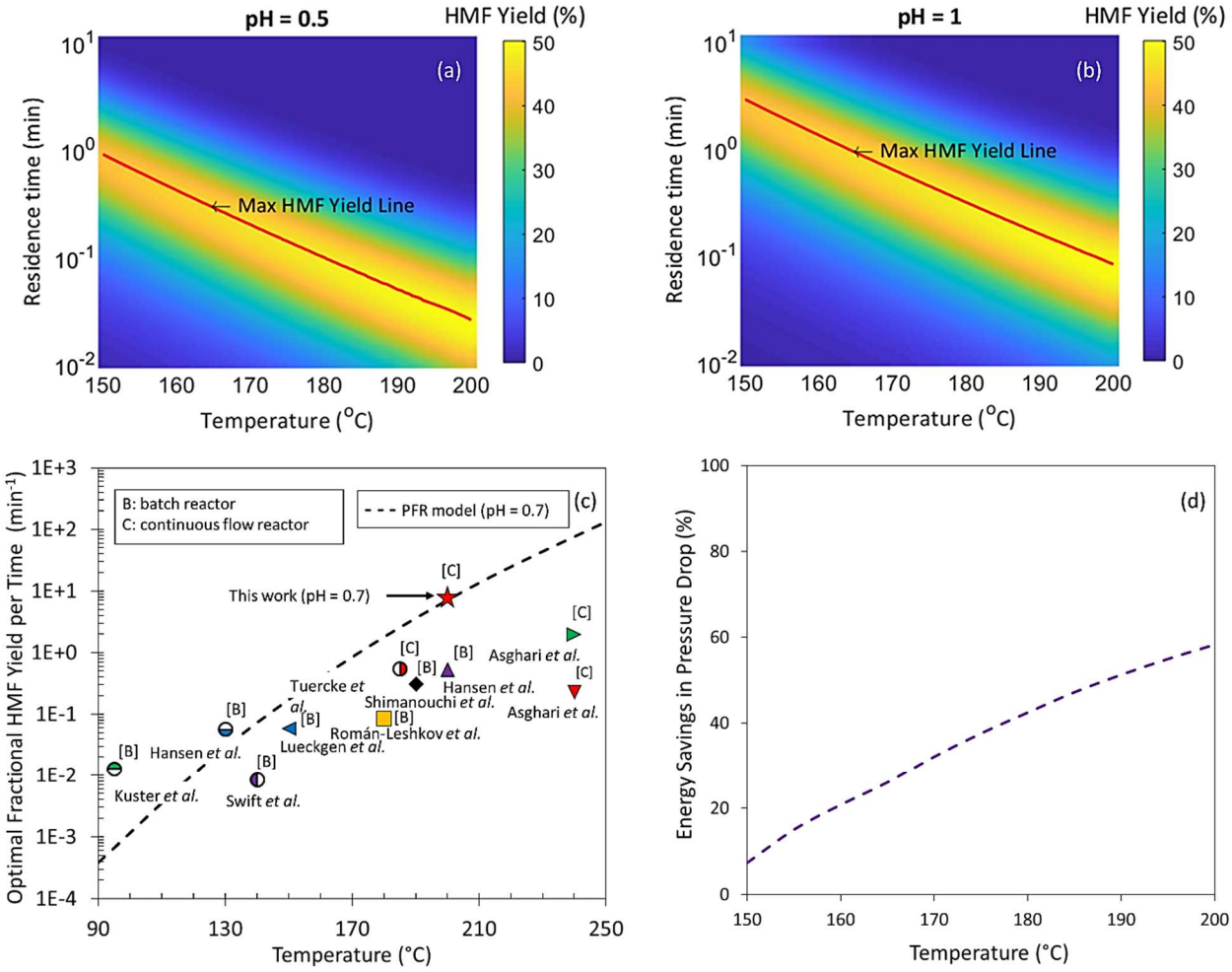

Figure 5d presents the estimated energy savings as a function of the reaction temperature. While the optimal flow rate increases with temperature, the optimal reactor length decreases with temperature in order to achieve the maximum HMF yield. Thereon, high temperatures not only improve productivity but also allow more compact microsystems, which reduce the capital cost for a target productivity. Furthermore, higher temperatures result in greater energy savings arising from pressure drop, from 7.4% at 150 °C up to 58.3% at 200 °C. These data show that, with proper design, it is possible to minimize the energy losses and make these systems sustainable while achieving processing at ultrashort residence times to improve the HMF yield from fructose.

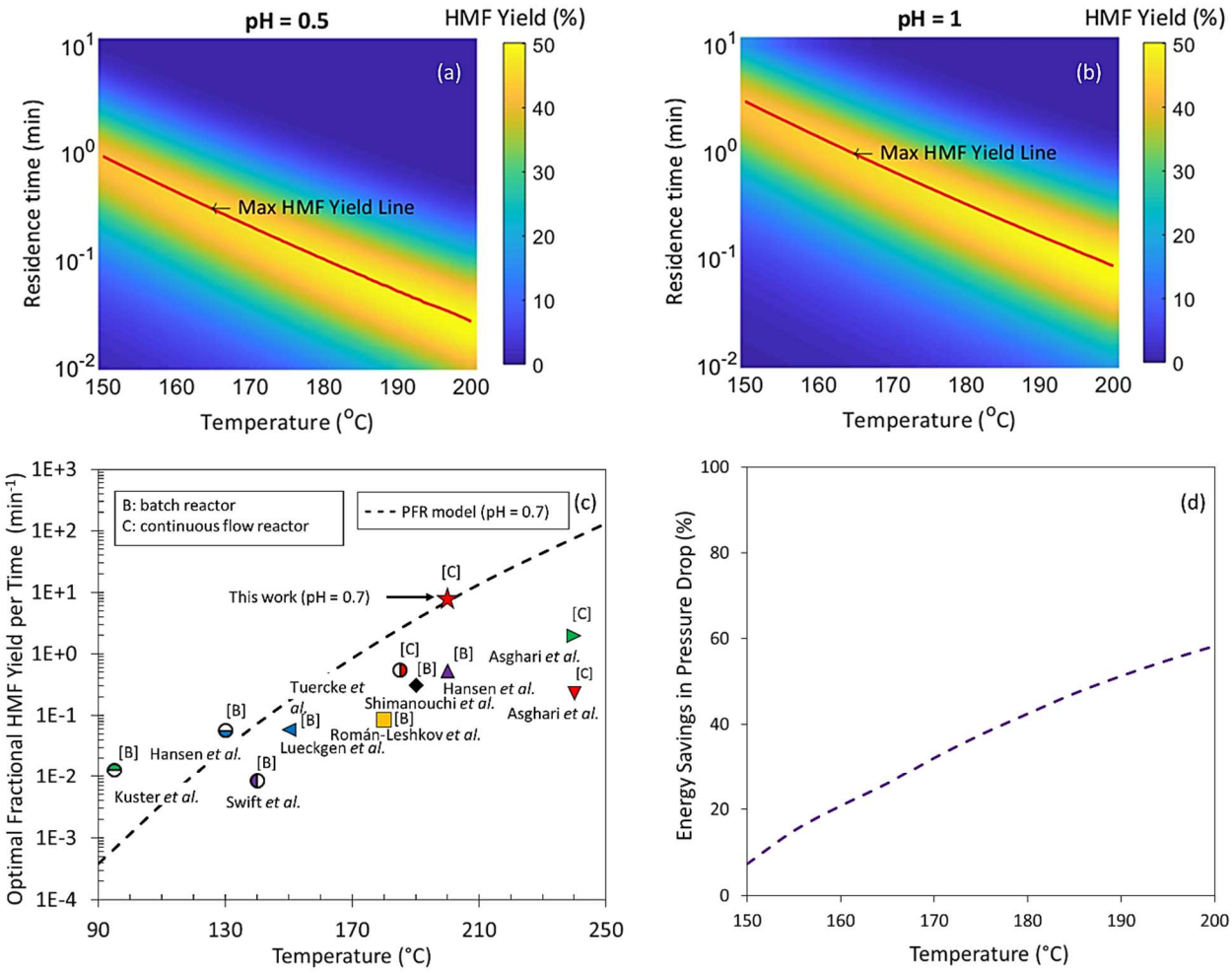

Figure 5: Kinetic model predictions for the HMF yield as a function of temperature and residence time at pH = 0.5 (a) and pH = 1 (b). The red line traces the max HMF yield. Optimal HMF fractional yield per time (c) obtained experimentally in the microreactor (red star) and derived from literature reports (Kuster *et al.* (half-filled green circle)[71], Hansen *et al.* (half-filled blue circle)[50], Swift *et al.* (half-filled magenta circle)[40], Tuercke *et al.* (half-filled red circle)[46], Hansen *et al.* (magenta triangle)[50], Lueckgen *et al.* (blue triangle)[70], Asghari *et al.* (red triangle)[72], Asghari *et al.* (green triangle)[73], Shimanouchi *et al.* (black diamond)[74], and Román-Leshkov and co-workers (yellow square)[75]) plotted at various temperatures for the single-phase HCl-catalyzed fructose dehydration in water. Model predictions of the energy savings (d) in the microreactor after optimization of the HMF yield, microreactor flow rate, length, and pressure drop with respect to temperature, at pH = 0.7.

Scalability

We developed a scale-up methodology of a microreactor by increasing its diameter to further enhance its throughput under optimal reaction conditions. To achieve this, we maintain the characteristic hydrodynamic behavior and fast mixing at the same residence time. We consider the dimensionless numbers De and Pe as they respectively govern vortex formation and mixing. To

preserve the fluid dynamics of the nominal microreactor, De and the curvature ratio $\left(\frac{d_H}{2R}\right)$ are kept constant during scale-up:

$$De_1 = De_2 \tag{13}$$

$$Re_1\sqrt{\frac{d_{H,1}}{2R_1}} = Re_2\sqrt{\frac{d_{H,2}}{2R_2}} \tag{14}$$

$$\frac{d_{H,1}}{2R_1} = \frac{d_{H,2}}{2R_2} \tag{15}$$

where the variables are as previously defined and the subscripts 1 and 2 correspond to the nominal microreactor (ID = 500 µm) and the scaled-up reactor, respectively. A direct consequence of equations (14) and (15) is that Re values are the same during scale-up:

$$Re_1 = Re_2 \tag{16}$$

$$U_1 d_{H,1} = U_2 d_{H,2} \tag{17}$$

$$\frac{U_2}{U_1} = \frac{d_{H,1}}{d_{H,2}} \tag{18}$$

Comparison of equations (10) and (17) suggests that the Pe number also remains constant:

$$Pe_1 = Pe_2 \tag{19}$$

The correlation in Figure 1d and equation (19) indicate that the mixing time t_{mix} is unchanged during scale-up when keeping De and the curvature constant.

Moreover, since $\frac{d_{H,1}}{d_{H,2}} < 1$, it follows that $U_2 < U_1$ according to equation (18). Since the residence time is constant during scale-up ($\tau_1 = \tau_2$), the reactor length is shortened $\left(L_{R,2} < L_{R,1}\right)$. When the reactor becomes too short, entrance effects become relevant and the flow is not fully developed, i.e., the hydrodynamics are no longer preserved. This behavior is described by the hydrodynamic length, L_H (equation (S9), ESI). When $\frac{L_H}{L_R} \leq 1$, the flow is fully developed and the hydrodynamics are preserved. When $\frac{L_H}{L_R} > 1$, the flow is developing, the hydrodynamics are not preserved, and the reactor cannot be scaled-up in the same manner.

Figure 6a shows $\frac{L_H}{L_R}$ and the scale-up factor, S, defined as:

$$S = \frac{V_{R,2}}{V_{R,1}} \tag{20}$$

as a function of the reactor diameter. Here $V_{R,1}$ and $V_{R,2}$ are the volumes of the nominal and scaled-up reactors, respectively. The microreactor can be scaled-up to millimeter size (of an internal diameter of 8 mm), corresponding to a 16-fold increase in reactor throughput at $\frac{L_H}{L_R} = 1$, while

maintaining both the hydrodynamics and mixing characteristics. Further increase in throughput can be achieved by scaling-out, i.e., by numbering up a sufficient number of 8 mm milli-reactors.

Overall Energy Efficiency

We estimated the overall energy efficiency in the range of reactor diameters from 0.5 to 8 mm, for an HMF target production of 2.5 metric tons per day, based on data gathered from the 2016 annual production of a Midwest farm (USDA NASS) of 600 acres of corn field and the highest yield of fructose obtained by enzymatic hydrolysis of corn stover[76, 77], one type of food waste. Using a 5 wt% fructose feed in water, single-feed reactors are numbered up as parallel tubes in a single-pass multitubular counter-current Shell-and-Tube heat exchanger (Hex) where saturated steam at 200 °C is used as the heating fluid in the shell side under conditions to achieve optimal HMF productivity. The overall energy efficiency of the process is calculated as the thermal efficiency of the Hex, assuming that the saturated steam is generated by burning natural gas. More details on the calculations can be found in Table S3, equations (S28) – (S38), ESI. Figure 6b shows the calculated number of reactors needed during the scale-out to meet the target production and the efficiency of the Hex as a function of each single reactor diameter. As the reactor diameter increases from 0.5 to 8 mm, the number of scaled-out channels decreases >10-fold (from 9,037 to 565) while the energy efficiency drops from 100% to about 60%. This data shows that, as we scale-up the microreactor to the millimeter scale, the enhanced throughput per reactor allows a smaller number of reactors to meet production. However, the overall heat transfer coefficient and the total surface area for heat transfer decrease, resulting in lower thermal efficiency and consequently in a drop of the operating temperature from its optimum point. Importantly, the number of micro- or milli-reactors needed for production at a single farm scale is relatively small and this need can easily be met by additive manufacturing.

Cost Analysis

We conducted a relative cost analysis for an envisioned mini-plant including a distillation column to separate HMF from the aqueous phase with 95% purity (Scheme S3, ESI). We sized the system and calculated a total capital investment for a preliminary estimate using the method of Guthrie (1974)[78] with a ±20% accuracy. By taking into account the heat transfer occurring in the Hex between the saturated steam and scaled-out channels, we modeled each single reactor as a non-isothermal plug flow reactor by incorporating the rate of change in the temperature profile along the reactor into the kinetic model. We then estimated the minimum price of HMF[79, 80] to make this process profitable. To our knowledge, this is one of the first examples where heat transfer limitations and temperature-dependent kinetics are accounted for in productivity and economic analysis. Details of the cost estimation are in Table S4 – Table S8, Figure S12 – Figure S13, and equations (S39) – (S41) in the ESI. Figure 6c plots the actual HMF production rate and HMF minimum price predicted for the non-isothermal reactors as a function of the reactor diameter for the target production.

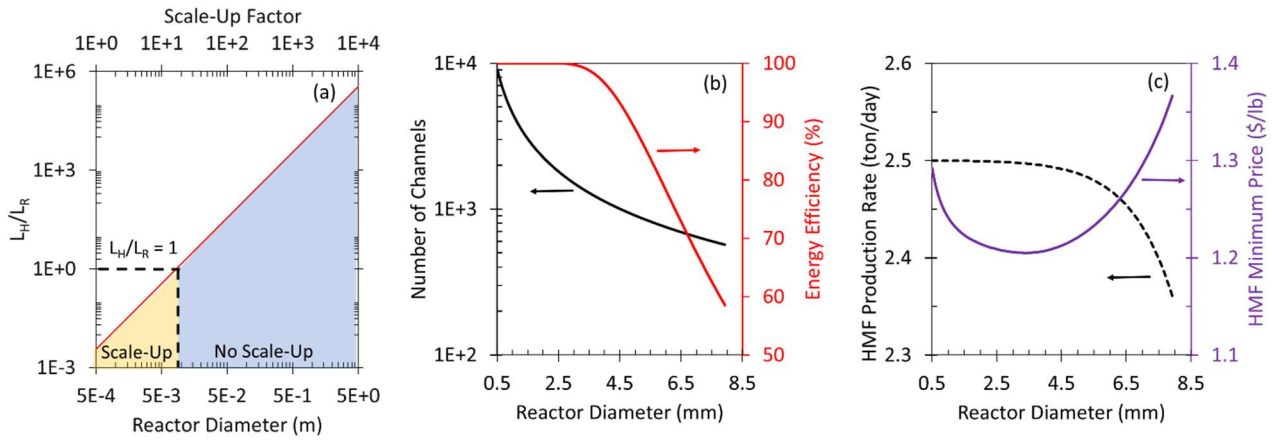

Figure 6: $\frac{L_H}{L_R}$ ratio as a function of the reactor diameter during scale-up (a). Number of channels and energy efficiency (b) and minimum selling price of HMF (c) vs. reactor diameter for a target HMF production of 2.5 ton/day under optimal reaction conditions.

Up to a reactor diameter of 3.5 mm (1,280 channels in parallel), the HMF production rate remains unchanged at 2.5/ton day and the HMF price reaches its lowest value of $1.20/lb while the energy efficiency remains unchanged at ~100% for optimal scale-up conditions. For these small sizes, the optimal reaction temperature of 200 °C and the short reaction time of 4 s are achieved. Above 3.5 mm, the HMF price increases because the energy efficiency decreases and the reactor temperature is lower than the optimal one, producing a lower yield of HMF at such short residence times. Interestingly, heat transfer to the reaction medium dominates over hydrodynamics in scaling-up the process. These economic estimates indicate that a sevenfold scale-up of the nominal (0.5 mm) microreactor is ideal for HMF production to achieve the lowest price. More extensive techno-economic analyses on HMF production from either glucose or fructose by reactive extraction in biphasic continuously stirred tank reactors (CSTR) or other conventional continuous reactors using miscible mixtures of organic solvent and water have shown HMF minimum selling prices in the range of $0.40/lb to $0.87/lb[77, 80-83]. Given the accuracy of our cost estimation[78] and the lower yield in the monophasic aqueous system, the HMF prices in milli-reactors operating at short contact times are comparable to previous reports in large scale reactors while demonstrating compact and remote operation. We expect an even more profitable technology by employing reactive extraction and recycling the unreacted fructose. Further cost reduction can be achieved (Figure S12 and Figure S13) by lower-cost sugars, as may be the case of farm waste, and better/cheaper energy sources, e.g., using farm-integrated renewable energy sources. Importantly, the number of reactors needed to perform this operation for a typical corn farm is relatively small, demonstrating the potential feasibility of this technology for remote production of bioproducts. While the cost of microsystems for other applications is typically high[84, 85], this is clearly not the case for biomass processing (Figure S13 and Table S8). Furthermore, the overall methodology proposed herein can be applied to other biomass processes.

Conclusions

We designed an aqueous-phase, coiled microreactor to enable ultrashort flow chemistry for biomass processing with the ultimate goal of enabling portable and distributed manufacturing of renewable chemicals and fuels. We demonstrated the system for the HCl-catalyzed fructose dehydration. We characterized and quantified the mixing and found that the coiled geometry induces Dean vortices by centrifugal forces, resulting into mixing times ranging from 0.03 to 4.8 s. PIV studies confirmed the formation of secondary vortices that enable partially chaotic mixing. Furthermore, the mixing time was shown to depend on the Péclet number and thus can be tuned. By mixing two separate streams (the catalyst and the substrate) of different flow rate and temperature, using a T-micromixer, we ensure temperature uniformity along the coiled microchannel while preventing fructose dehydration prior to mixing with the acid catalyst. This design is also ideal for measuring isothermal kinetics at short residence times, something that has not been possible in prior biomass work. Since the microreactor design is void of transport limitations, we further investigated the intrinsic kinetics of fructose dehydration using an HCl/KCl buffer catalyst and compared the experimental results to a hybrid first principles/data-driven kinetic model. The model predicts the experimental data adequately despite its significant extrapolation. The model was used to obtain the attainable operating region and to optimize the yield of HMF. The optimal region is rather broad enabling robust operation. The predicted optimal HMF yield in single-(aqueous) phase of ~50% is close to the 54% value obtained experimentally. Due to short residence times and high temperatures, our results demonstrate the highest ever productivity achieved to date. Productivity could possibly be further enhanced by increasing the temperature and/or lowering the pH. We also estimated the shortest microchannel length to maximize the HMF yield while minimizing the pressure drop and energy expenditure and assuring fast mixing at various temperatures, resulting in ~60% savings from pressure drop. Furthermore, we established a methodology to scale-up the microreactor under optimal conditions while maintaining the characteristic fluid dynamics and mixing properties, achieving a 16-fold increase in reactor size (a millimeter reactor of ID = 8 mm), relatively to the nominal microreactor. We then considered the numbering-up or scaling-out of these reactors for small-scale HMF production for on-site processing of corn stover waste from a corn field and demonstrated that a relatively small number of reactors is needed, indicating for the first time that remote and distributed manufacturing of biomass is feasible. Heat transfer dominates over hydrodynamics in the scale-up. Cost analysis reveals that the lowest HMF minimum selling price ($1.20/lb) is obtained by scaling-up the microreactor sevenfold (millimeter reactor of ID = 3.5 mm) with ~100% thermal efficiency. CFD modeling in combination with experimental heat transfer, hydrodynamic, and mixing studies along with detailed techno-economic analysis can guide process intensification for the pursuit of industrial production of renewable fuels from biomass. The relative cost analysis underscores that development and deployment of microreactor technology for HMF production at the farm-scale will benefit from a cheaper fructose feedstock and from energy efficiency and faster heating to drive down the total capital investment. The former may be possible from leftover farm waste and the latter may be achievable using alternative energy sources.

Conflicts of interest
There are no conflicts to declare.

Acknowledgements
This work was supported by the National Science Foundation (NSF) under the SusChem Collaborative Research, with award number 1434456. The microchannel optimization studies were supported by the RAPID manufacturing institute, supported by the Department of Energy (DOE), award number DE-EE0007888-7.6.

References
1. M. Chidambaram and A. T. Bell, *Green Chemistry*, 2010, **12**, 1253-1262.
2. L. Hu, G. Zhao, W. W. Hao, X. Tang, Y. Sun, L. Lin and S. J. Liu, *Rsc Advances*, 2012, **2**, 11184-11206.
3. X. L. Tong, Y. Ma and Y. D. Li, *Applied Catalysis a-General*, 2010, **385**, 1-13.
4. J. M. R. Gallo, D. M. Alonso, M. A. Mellmer and J. A. Dumesic, *Green Chemistry*, 2013, **15**, 85-90.
5. Y. H. Zu, P. P. Yang, J. J. Wang, X. H. Liu, J. W. Ren, G. Z. Lu and Y. Q. Wang, *Applied Catalysis B-Environmental*, 2014, **146**, 244-248.
6. G. H. Wang, J. Hilgert, F. H. Richter, F. Wang, H. J. Bongard, B. Spliethoff, C. Weidenthaler and F. Schuth, *Nature Materials*, 2014, **13**, 294-301.
7. N. Nikbin, S. T. Feng, S. Caratzoulas and D. G. Vlachos, *Journal of Physical Chemistry C*, 2014, **118**, 24415-24424.
8. R. E. Patet, N. Nikbin, C. L. Williams, S. K. Green, C. C. Chang, W. Fan, S. Caratzoulas, P. J. Dauenhauer and D. G. Vlachos, *Acs Catalysis*, 2015, **5**, 2367-2375.
9. C. L. Williams, K. P. Vinter, C. C. Chang, R. C. Xiong, S. K. Green, S. I. Sandler, D. G. Vlachos, W. Fan and P. J. Dauenhauer, *Catalysis Science & Technology*, 2016, **6**, 178-187.
10. C. L. Williams, K. P. Vinter, R. E. Patet, C. C. Chang, N. Nikbin, S. T. Feng, M. R. Wiatrowski, S. Caratzoulas, W. Fan, D. G. Vlachos and P. J. Dauenhauer, *Acs Catalysis*, 2016, **6**, 2076-2088.
11. R. C. Xiong, S. I. Sandler, D. G. Vlachos and P. J. Dauenhauer, *Green Chemistry*, 2014, **16**, 4086-4091.
12. N. Nikbin, P. T. Do, S. Caratzoulas, R. F. Lobo, P. J. Dauenhauer and D. G. Vlachos, *Journal of Catalysis*, 2013, **297**, 35-43.
13. C. L. Williams, C. C. Chang, P. Do, N. Nikbin, S. Caratzoulas, D. G. Vlachos, R. F. Lobo, W. Fan and P. J. Dauenhauer, *Acs Catalysis*, 2012, **2**, 935-939.
14. C. C. Chang, S. K. Green, C. L. Williams, P. J. Dauenhauer and W. Fan, *Green Chemistry*, 2014, **16**, 585-588.
15. R. E. Patet, W. Fan, D. G. Vlachos and S. Caratzoulas, *Chemcatchem*, 2017, **9**, 2523-2535.
16. C. C. Chang, H. J. Cho, J. Y. Yu, R. J. Gorte, J. Gulbinski, P. Dauenhauer and W. Fan, *Green Chemistry*, 2016, **18**, 1368-1376.

17. R. E. Patet, M. Koehle, R. F. Lobo, S. Caratzoulas and D. G. Vlachos, *Journal of Physical Chemistry C*, 2017, **121**, 13666-13679.
18. H. J. Cho, L. M. Ren, V. Vattipalli, Y. H. Yeh, N. Gould, B. J. Xu, R. J. Gorte, R. Lobo, P. J. Dauenhauer, M. Tsapatsis and W. Fan, *Chemcatchem*, 2017, **9**, 398-402.
19. O. A. Abdelrahman, D. S. Park, K. P. Vinter, C. S. Spanjers, L. Ren, H. J. Cho, D. G. Vlachos, W. Fan, M. Tsapatsis and P. J. Dauenhauer, *ACS Sustainable Chemistry & Engineering*, 2017, **5**, 3732-3736.
20. D. S. Park, K. E. Joseph, M. Koehle, C. Krumm, L. M. Ren, J. N. Damen, M. H. Shete, H. S. Lee, X. B. Zuo, B. Lee, W. Fan, D. G. Vlachos, R. F. Lobo, M. Tsapatsis and P. J. Dauenhauer, *Acs Central Science*, 2016, **2**, 820-824.
21. S. E. Davis, L. R. Houk, E. C. Tamargo, A. K. Datye and R. J. Davis, *Catalysis Today*, 2011, **160**, 55-60.
22. S. E. Davis, B. N. Zope and R. J. Davis, *Green Chemistry*, 2012, **14**, 143-147.
23. M. Kroger, U. Prusse and K. D. Vorlop, *Topics in Catalysis*, 2000, **13**, 237-242.
24. S. B. Liu, T. R. Josephson, A. Athaley, Q. P. Chen, A. Norton, M. Ierapetritou, J. I. Siepmann, B. Saha and D. G. Vlachos, *Science Advances*, 2019, **5**.
25. J. S. Kruger, V. Choudhary, V. Nikolakis and D. G. Vlachos, *Acs Catalysis*, 2013, **3**, 1279-1291.
26. M. Leon, T. D. Swift, V. Nikolakis and D. G. Vlachos, *Langmuir*, 2013, **29**, 6597-6605.
27. M. E. Davis, *Topics in Catalysis*, 2015, **58**, 405-409.
28. M. Moliner, Y. Roman-Leshkov and M. E. Davis, *Proceedings of the National Academy of Sciences of the United States of America*, 2010, **107**, 6164-6168.
29. T. D. Swift, H. Nguyen, Z. Erdman, J. S. Kruger, V. Nikolakis and D. G. Vlachos, *Journal of Catalysis*, 2016, **333**, 149-161.
30. S. Dutta, S. De, A. K. Patra, M. Sasidharan, A. Bhaumik and B. Saha, *Applied Catalysis a-General*, 2011, **409**, 133-139.
31. X. H. Qi, M. Watanabe, T. M. Aida and R. L. Smith, *Catalysis Communications*, 2008, **9**, 2244-2249.
32. M. Watanabe, Y. Aizawa, T. Iida, T. M. Aida, C. Levy, K. Sue and H. Inomata, *Carbohydrate Research*, 2005, **340**, 1925-1930.
33. X. H. Qi, M. Watanabe, T. M. Aida and R. L. Smith, *Catalysis Communications*, 2009, **10**, 1771-1775.
34. C. Aellig and I. Hermans, *Chemsuschem*, 2012, **5**, 1737-1742.
35. C. Lansalot-Matras and C. Moreau, *Catalysis Communications*, 2003, **4**, 517-520.
36. V. V. Ordomsky, J. van der Schaaf, J. C. Schouten and T. A. Nijhuis, *Chemsuschem*, 2012, **5**, 1812-1819.
37. K. Shimizu, R. Uozumi and A. Satsuma, *Catalysis Communications*, 2009, **10**, 1849-1853.
38. B. Girisuta, L. Janssen and H. J. Heeres, *Green Chemistry*, 2006, **8**, 701-709.
39. S. K. R. Patil and C. R. F. Lund, *Energy & Fuels*, 2011, **25**, 4745-4755.
40. T. D. Swift, C. Bagia, V. Choudhary, G. Peklaris, V. Nikolalds and D. G. Vlachos, *Acs Catalysis*, 2014, **4**, 259-267.
41. T. D. Swift, H. Nguyen, A. Anderko, V. Nikolakis and D. G. Vlachos, *Green Chemistry*, 2015, **17**, 4725-4735.

42. A. V. Bridgewater and Imeche, in *Renewable Bioenergy - Technologies, Risks and Rewards*, 2003, vol. 2003, pp. 33-61.
43. M. S. Mettler, D. G. Vlachos and P. J. Dauenhauer, *Energy & Environmental Science*, 2012, **5**, 7797-7809.
44. A. Oasmaa and S. Czernik, *Energy & Fuels*, 1999, **13**, 914-921.
45. A. Oasmaa and D. Meier, *Journal of Analytical and Applied Pyrolysis*, 2005, **73**, 323-334.
46. T. Tuercke, S. Panic and S. Loebbecke, *Chemical Engineering & Technology*, 2009, **32**, 1815-1822.
47. K. Jahnisch, V. Hessel, H. Lowe and M. Baerns, *Angewandte Chemie-International Edition*, 2004, **43**, 406-446.
48. B. P. Mason, K. E. Price, J. L. Steinbacher, A. R. Bogdan and D. T. McQuade, *Chemical Reviews*, 2007, **107**, 2300-2318.
49. T. M. Aida, K. Tajima, M. Watanabe, Y. Saito, K. Kuroda, T. Nonaka, H. Hattori, R. L. Smith and K. Arai, *Journal of Supercritical Fluids*, 2007, **42**, 110-119.
50. T. S. Hansen, J. M. Woodley and A. Riisager, *Carbohydrate Research*, 2009, **344**, 2568-2572.
51. W. Thielicke and E. J. Stamhuis, *Journal of Open Research Software*, 2014, **2**.
52. S. Caratzoulas and D. G. Vlachos, *Carbohydrate Research*, 2011, **346**, 664-672.
53. N. Nikbin, S. Caratzoulas and D. G. Vlachos, *Chemcatchem*, 2012, **4**, 504-511.
54. T. J. Johnson, D. Ross and L. E. Locascio, *Analytical Chemistry*, 2002, **74**, 45-51.
55. M. K. Gelber, M. R. Kole, N. Kim, N. R. Aluru and R. Bhargava, *Analytical Chemistry*, 2017, **89**, 1716-1723.
56. A. A. S. Bhagat, S. S. Kuntaegowdanahalli and I. Papautsky, *Lab on a Chip*, 2008, **8**, 1906-1914.
57. N. Nivedita, P. Ligrani and I. Papautsky, *Scientific Reports*, 2017, **7**.
58. K. J. Cook, Y. F. Fan and I. Hassan, *Journal of Fluids Engineering-Transactions of the Asme*, 2013, **135**.
59. A. D. Stroock, S. K. W. Dertinger, A. Ajdari, I. Mezic, H. A. Stone and G. M. Whitesides, *Science*, 2002, **295**, 647-651.
60. J. M. Ottino and S. Wiggins, *Philosophical Transactions of the Royal Society of London Series a-Mathematical Physical and Engineering Sciences*, 2004, **362**, 923-935.
61. M. Giona, S. Cerbelli and V. Vitacolonna, *Journal of Fluid Mechanics*, 2004, **513**, 221-237.
62. J. P. Gleeson, *Physics of Fluids*, 2005, **17**.
63. H. J. Kim and A. Beskok, *Journal of Micromechanics and Microengineering*, 2007, **17**, 2197-2210.
64. G. Froyland and K. Padberg, *Physica D-Nonlinear Phenomena*, 2009, **238**, 1507-1523.
65. G. Elert, The chaos hypertextbook : mathematics in the age of the computer, http://hypertextbook.com/chaos/.
66. M. Bicker, D. Kaiser, L. Ott and H. Vogel, *Journal of Supercritical Fluids*, 2005, **36**, 118-126.
67. R. Weingarten, J. Cho, R. Xing, W. C. Conner and G. W. Huber, *Chemsuschem*, 2012, **5**, 1280-1290.

68. S. Y. Jia, K. R. Liu, Z. W. Xu, P. F. Yan, W. J. Xu, X. M. Liu and Z. C. Zhang, *Catalysis Today*, 2014, **234**, 83-90.
69. C. J. Zhou, C. Shen, K. Y. Ji, J. B. Yin and L. Dut, *Acs Sustainable Chemistry & Engineering*, 2018, **6**, 3992-3999.
70. J. Lueckgen, L. Vanoye, R. Philippe, M. Eternot, P. Fongarland, C. de Bellefon and A. Favre-Reguillon, *Journal of Flow Chemistry*, 2018, **8**, 3-9.
71. B. F. M. Kuster and H. S. Vanderbaan, *Carbohydrate Research*, 1977, **54**, 165-176.
72. F. S. Asghari and H. Yoshida, *Industrial & Engineering Chemistry Research*, 2006, **45**, 2163-2173.
73. F. S. Asghari and H. Yoshida, *Industrial & Engineering Chemistry Research*, 2007, **46**, 7703-7710.
74. T. Shimanouchi, Y. Kataoka, T. Tanifuji, Y. Kimura, S. Fujioka and K. Terasaka, *Aiche Journal*, 2016, **62**, 2135-2143.
75. Y. Roman-Leshkov, J. N. Chheda and J. A. Dumesic, *Science*, 2006, **312**, 1933-1937.
76. H. Li, S. Yang, S. Saravanamurugan and A. Riisager, *Acs Catalysis*, 2017, **7**, 3010-3029.
77. M. Galbe and G. Zacchi, in *Biofuels*, ed. L. Olsson, 2007, vol. 108, pp. 41-65.
78. W. D. Seider, *Product and process design principles : synthesis, analysis, and evaluation*, John Wiley, Hoboken, NJ, 2009.
79. A. I. Torres, M. Tsapatsis and P. Daoutidis, *Computers & Chemical Engineering*, 2012, **42**, 130-137.
80. A. I. Torres, P. Daoutidis and M. Tsapatsis, *Energy & Environmental Science*, 2010, **3**, 1560-1572.
81. F. K. Kazi, A. D. Patel, J. C. Serrano-Ruiz, J. A. Dumesic and R. P. Anex, *Chemical Engineering Journal*, 2011, **169**, 329-338.
82. Z. J. Lin, J. Y. Wang, V. Nikolakis and M. Ierapetritou, *Computers & Chemical Engineering*, 2017, **102**, 258-267.
83. A. H. Motagamwala, K. Huang, C. T. Maravelias and J. A. Dumesic, *Energy & Environmental Science*, 2019.
84. C. Bramsiepe, S. Sievers, T. Seifert, G. D. Stefanidis, D. G. Vlachos, H. Schnitzer, B. Muster, C. Brunner, J. P. M. Sanders, M. E. Bruins and G. Schembecker, *Chem. Eng. Processing: Process Intensification*, 2012, **51**, 32– 52.
85. M. S. Mettler, G. D. Stefanidis and D. G. Vlachos, *Ind. Eng. Chem. Res.*, 2010, **49**, 10942–10955.